In situ EPR study of the redox properties of $CuO–CeO_2$ catalysts for the preferential CO oxidation (PROX)

Feng Wang[1], Robert Büchel[2], Anton Savitsky[3], Michal Zalibera[3], Daniel Widmann[4], Sotiris E. Pratsinis[2], Wolfgang Lubitz[3], Ferdi Schüth[1*]

[1]Max-Planck-Institut für Kohlenforschung, Kaiser-Wilhelm-Platz 1, D-45470 Mülheim an der Ruhr, Germany, [2]Department of Mechanical and Process Engineering, ETH Zürich, 8092 Zürich, Switzerland, [3]Max-Planck-Institut für Chemische Energiekonversion, Stiftstrasse 34–36, 45470 Mülheim an der Ruhr, Germany
[4]Ulm University, Institute of Surface Chemistry & Catalysis, D-89069 Ulm, Germany
*E-mail: sotiris.pratsinis@ptl.mavt.ethz.ch, wolfgang.lubitz@cec.mpg.de, schueth@kofo.mpg.de, Tel: +49(0)208/306-2373

Abstract

Understanding the redox properties of metal oxide based catalysts is a major task in catalysis research. *In situ* Electron Paramagnetic Resonance (EPR) spectroscopy is capable to monitor the change of metal ion valences and formation of active sites during redox reactions, allowing for the identification of ongoing redox pathways. Here *in situ* EPR spectroscopy combined with online gas analysis, supported by *ex situ* X-ray photoelectron spectroscopy (XPS), X-ray diffraction (XRD), X-ray absorption near edge structure (XANES), temporal analysis of product (TAP), mass spectrometry (MS) studies was utilized to study the redox behavior of $CuO–CeO_2$ catalysts under PROX conditions (preferential oxidation of carbon monoxide in hydrogen). Two redox mechanisms are revealed: (i) a *synergetic mechanism* that involves the redox pair Ce^{4+}/Ce^{3+} during oxidation of Cu^0/Cu^+ species to Cu^{2+}, and (ii) a *direct mechanism* that bypasses the redox pair Ce^{4+}/Ce^{3+}. In addition, EPR experiments with isotopically enriched $^{17}O_2$ established the *synergetic mechanism* as the major redox reaction pathway. The results emphasize the importance of the interactions between Cu and Ce atoms for catalyst performance. Guided by these results an optimized $CuO\text{-}CeO_2$ catalyst could be designed. A rather wide temperature operation window of 11 degrees (from 377 K to 388 K), with 99% conversion efficiency and 99% selectivity was achieved for the preferential oxidation of CO in a H_2 feed.

Key Words: $CuO\text{-}CeO_2$ catalyst, *in situ* spectroscopy, EPR, redox mechanism, preferential CO oxidation

1. INTRODUCTION

Metal oxides, in particular ceria and copper oxides, are widely used as catalysts or catalyst supports due to their rich redox properties.[1-3] Ceria, for example, is well known for its oxygen storage and transfer capacity, and has been applied as an oxygen storage compound in the automotive three-way catalytic converter for gasoline engines.[4] Copper and its oxides, CuO and Cu_2O, offer redox reactions involving three valence states at relatively low temperatures. These can serve as catalytically active components in water gas shift and methanol synthesis catalysts.[5,6] The combination of ceria and copper establishes a unique system with rich redox properties and attractive oxygen storage capacities. It represents the benchmark catalyst for the water gas shift reaction,[2,7] the preferential CO oxidation,[8,9] and, recently, also the methanol synthesis.[10] Due to its many applications, the redox behavior of $CuO\text{-}CeO_2$ has been studied intensively under *ex situ* and *in situ* conditions over the last 20 years.[11-14] The common understanding of the redox behavior, for instance, in CO oxidation, is:

$$2Cu^{2+} + CO + O^{2-} \leftrightharpoons 2Cu^{+} + CO_2 \text{ and/or } Cu^{2+} + CO + O^{2-} \leftrightharpoons Cu^{0} + CO_2 \qquad (1)$$

$$2\,Cu^{+} + 2Ce^{4+} \leftrightharpoons 2Cu^{2+} + 2Ce^{3+} \text{ and/or } Cu^{0} + 2Ce^{4+} \leftrightharpoons Cu^{2+} + 2Ce^{3+} \qquad (2)$$

$$2Ce^{3+} + \frac{1}{2}O_2 \leftrightharpoons 2Ce^{4+} + O^{2-} \qquad (3)$$

Starting with a fully oxidized catalyst ($CuO\text{-}CeO_2$), CO abstracts an O^{2-} from Cu^{2+} and is oxidized to CO_2. Simultaneously, this reaction results in the formation of 2 Cu^{+} or Cu^{0} from Cu^{2+} (eq. 1). In the second step, the newly formed Cu^{+} or Cu^{0} is reoxidized by Ce^{4+}, forming Cu^{2+} and Ce^{3+} (eq. 2). In the last step, Ce^{3+} is finally reoxidized into Ce^{4+} by O_2 (eq. 3), and the catalyst is again in its initial state (fully oxidized). Accordingly, both redox pairs, Cu^{2+}/Cu^{+} and Ce^{4+}/Ce^{3+},

directly participate in this mechanism. Since Cu and Ce work in a cooperative manner, it is called the "*synergetic mechanism*".[15] Oxygen enters the CeO_2 lattice, migrates to the neighborhood of a Cu-site, and then binds with CO to form CO_2. However, it may also be possible that Cu^+ or Cu^0 are directly reoxidized to Cu^{2+} by O_2 from the gas phase, bypassing the Ce^{4+}/Ce^{3+} redox pair (eq. 4). In this case, Cu solely serves as the active species, and this reaction pathway is correspondingly called the "*direct mechanism*". Here oxygen enters only a specific Cu site and is directly removed by reaction with CO.

$$2Cu^{+} + \frac{1}{2}O_2 \leftrightharpoons 2Cu^{2+} + O^{2-} \text{ and/or } 2Cu^{0} + O_2 \leftrightharpoons 2Cu^{2+} + 2O^{2-} \qquad (4)$$

Both the *synergetic* and the *direct mechanism* may be relevant in redox reactions and their relative contributions are still not clear.[16,17] One possibility to distinguish between these mechanisms is via *in situ* spectroscopic experiments that enable the identification of valence states of metal ions/atoms. Electron paramagnetic resonance (EPR), in particular, gives detailed information on the presence of metal ions with unpaired electrons and is hence suitable for systematic mechanistic studies. However, EPR spectra for CuO-CeO_2 systems have so far been reported only for temperatures in the range from 77 K to room temperature.[18-22] Cu monomer and dimer signals were identified in the spectra recorded at room temperature. Moreover, the intensity of these signals decreased significantly when the sample was reduced at 573 K and cooled down to room temperature.[19] In addition, the Cu dimers were suggested to represent the active species for CO oxidation.[22] It is obviously important and challenging to study the reduction and reoxidation of these Cu species, and to determine whether oxygen reacts with Ce^{3+} or Cu^0/Cu^+ only, or with both of them. These studies, however, need to be performed *in situ* in order to gain relevant information about the mechanisms under working conditions. Note that

spectra recorded under reaction conditions, at 473 K and during exposure to reductive or oxidative gas atmospheres, have not yet been reported to the best of our knowledge.

This is topic of the present manuscript, in which an *in situ* EPR study[23] of the redox properties of CuO-CeO_2 under reaction conditions is presented. For this purpose a common quartz glass reactor was installed inside the EPR cavity and coupled with an online gas composition analysis. This reactor is manufactured from three quartz tubes forming a reaction channel, a heating gas channel and a thermal isolation dewar. A maximum sample temperature of 523 K can be reached in the reactor (SI Figure S1). CuO-CeO_2 materials are produced via flame spray pyrolysis, a method which allows synthesis of nanoparticles with controlled size[24] and support properties.[25] *In situ* EPR enables the direct observation of changes of the Cu^{2+} species and their correlation with changes of the catalyst structure and reaction kinetics. In combination with online real time gas composition analysis, *ex situ* X-ray photoelectron spectroscopy (XPS), X-ray diffraction (XRD), X-ray absorption near edge structure (XANES), mass spectrometry (MS) and temporal analysis of products (TAP) reactor studies, these measurements reveal that the (preferential oxidation) PROX reaction proceeds via both *synergetic* and *direct mechanisms*, with the *synergetic mechanism* being dominant under present reaction conditions. A highly active catalyst, hence, requires a large interface and strong interaction between CuO and CeO_2. These findings served as a guideline to optimize the CuO-CeO_2 catalyst for redox reactions under similar conditions, resulting in a significantly improved catalyst with a 11 degrees temperature operation window (ranging from 377 K to 388 K) in which 99% conversion and 99% selectivity in the preferential oxidation of CO in excess of H_2 feed gas were achieved.

2. Materials and Methods

2.1 Chemicals and synthesis of CuO-CeO_2.

The CuO-CeO_2 composites were prepared using the flame spray pyrolysis method[26]. The Cu/Ce-precursor solutions with different Cu:Ce ratio were prepared by mixing appropriate amounts of cerium-acetylacetonate (Sigma Aldrich) with copper-2-ethylhexanoate (Sigma Aldrich) in a solution of acetic acid (Fluka, >98.5%), methanol (Sigma Aldrich, 99.9%) and xylene (Sigma Aldrich, 95%) (25% vol. acetic acid, 25% vol. methanol and 50% vol. xylene). The resulting total metal concentration was 0.1 mol/L. These precursor solutions were sprayed at 2 ml/min, dispersed with 8 L/min O_2 (Pangas, 99,95%), and ignited by a premixed CH_4/O_2 ring-shaped flamelet (SI Figure S2, flow rates 1 L/min and 2 L/min, respectively). The resulting flame-made materials were collected from the filter and were not subject of additional temperature treatment. CuO-CeO_2 materials with CuO content of 1, 5, 20, 30, 40 wt% (based on the weight percentage of CuO in the whole materials) were made by tailoring the ratio between copper-2-ethylhexanoate and cerium-acetylacetonate. Different CuO-CeO_2 particle sizes (from approximately 4 ± 1 to 30 ± 4 nm) were realized by tailoring the ratio between the feed rates[24] of the precursor solution and the dispersion gas O_2.

2.2 Analytical instrumentation.

Nitrogen adsorption–desorption isotherms were measured at 77 K (Micromeritics Tristar), and the BET method was used to determine the specific surface area (SSA) by a 5-point nitrogen adsorption isotherm. The estimated accuracy is ±3%. XRD patterns were recorded with a Bruker D8 Advance instrument (40 kV, 40 mA, $\lambda = 0.154$ nm). Crystallite sizes were calculated using the fundamental parameter approach and the Rietveld method with the TOPAS 3 software at ±10% accuracy. Transmission electron microscopy (TEM) imaging was carried out on a Hitachi H7100. Scanning electron microscopy (SEM), correlated scanning transmission electron

microscopy (STEM), and element mapping were performed on a Hitachi S-5500 STEM. XPS analyses were performed on a Kratos His spectrometer with a hemispherical analyzer. The monochromatized Al Kα X-ray source (E=1486.6 eV) was operated at 15 kV and 15 mA. The analyzer pass energy of 40 eV was applied for the narrow scans. The hybrid mode was used as lens mode. The base pressure during the experiment in the analysis chamber was 4×10^{-7} Pa. Temperature programmed reduction (TPR) was performed on a Micromeritics AutoChemII 2920. The signal was calibrated by using a loop injection of H_2 gas. The data were collected at a ramp of 10 K per minute. XANES analysis was performed by transmission mode in an air tight chamber at room temperature on the B18 beamline of the Diamond Light Source (UK). Spectra were recorded in the range of 8.8 ~ 9.1 keV for Cu K edge and 5.5 ~ 6.1 keV for Ce L_3 edge. Cu and Ce spectra were calibrated based on the Cu and Cr foil, respectively. The Ce^{3+} concentrations were determined by peaking fitting according to a reported method[27,28] which involves a combination of Lorentzians and an arctangent function.

2.3 Catalytic evaluation methods.

(i) Pulse experiments in the TAP setup.

Pulse experiments were performed in a home-built TAP reactor, consisting of a gas mixing unit, two independently working piezo-electrically driven pulse valves and a tubular quartz glass micro reactor (90 mm long, 4.0 mm i.d., 6.0 mm o.d.), which is connected to an ultrahigh vacuum system (analysis chamber) via a differentially pumped gate valve. Here, the catalyst can first be pre-treated *in situ*, under continuous flow at atmospheric pressure, before the micro reactor is evacuated and directly connected to the analysis chamber. In this study the as-synthesized CuO-CeO_2 materials were calcined *in-situ* in a continuous flow of 10% O_2/N_2 at atmospheric pressure for 2 hours at 493 K (heating and cooling in Ar).

With the piezo-electric valves, gas pulses of typically 1×10^{16} molecules per pulse were injected into the micro reactor, in which the catalyst bed was fixed by stainless-steel sieves. After passing through the catalyst bed the effluent gases were analyzed by a MS located in the analysis chamber.

Oxygen isotope exchange between gas phase oxygen and the catalyst surface in a temperature range from 393–473 K was investigated by multi-pulse experiments, exposing the freshly calcined and, hence, fully oxidized CuO-CeO_2 materials (10 mg, diluted 1:2 with SiO_2 and packed between two layers of 60 mg SiO_2) at 393 K and 473 K to sequences of O_2/Ar pulses (45% $^{18}O_2$, 4% $^{18}O^{16}O$, 1% $^{16}O_2$, and 50% Ar) with a separation time of 12 s between individual pulses. SiO_2 as well as the metal sieves were checked to be inactive for oxygen isotope exchange under the reaction conditions applied (393–473 K).

(ii) PROX activity evaluation.

The catalytic activity for CO-PROX in H_2-rich gases was measured in a conventional fixed bed reactor (SI Figure S3) using a fixed amount of 50 mg of catalyst (grain size 250 ~ 500 μm, mixed with 200 mg quartz sand) in a gas mixture of 1.0 vol.% CO, 1.0 vol.% O_2, 50 vol.% H_2 and N_2 balance (total flow rate 50 mL/min). This results in a weight hourly space velocity (WHSV) of 60,000 $mL\cdot h^{-1}\cdot g^{-1}$. The catalysts were initially activated *in situ* at 573 K in a sequence of synthetic air (20 vol.% O_2 / 80 vol.% N_2, Air Liquide) for 60 min, 20 vol.% H_2 in N_2 for 40 min, and again synthetic air for 60 min. The concentrations of CO and CO_2 were analyzed with nondispersive infrared (IR) spectroscopy, and O_2 was analyzed with a paramagnetic analyzer at the outlet of the reactor using URAS 3E analyzers (ABB, EL3020, Hartmann and Braun). At each temperature measured, the reaction was performed for 30 min in order to reach a

steady-state condition. With catalyst weights between 5 and 50 mg the WHSV was varied between 600,000 and 60,000 $mL \cdot h^{-1} \cdot g^{-1}$.

(iii) EPR experiments.

All X-band EPR experiments were performed in continuous-wave (cw) mode on a Bruker Elexsys E580 X-band EPR spectrometer equipped with a Bruker ER4122-SHQE cavity, accommodating a gas flow reactor for *in situ* measurements. The home-build reactor (SI Figure S1) consists of a double-wall dewar manufactured from two tubes (10 mm o.d., 8 mm i.d.; 6.5 mm o.d., 5.5 mm i.d.) of high purity quartz (ilmasil PI, QSIL, Germany) and a quartz sample tube (3.8 mm o.d., 2.8 mm i.d.). The required sample temperature was set by regulating a heated dry nitrogen gas flow between the outer wall of the sample tube and the inner wall of the dewar. The system allows for a maximum sample temperature of 523 K. The sample temperature was controlled by a thermocouple positioned above the sample outside the EPR cavity. The reaction gas mixture was supplied from the upper inlet of the sample tube, and after passing the catalyst was directed to the gas analysis system. The gas control and analytic hardware for PROX evaluation (see above) was also used in the EPR experiments. All experiments were performed with ~80 mg $CuO\text{-}CeO_2$ catalyst placed inside the sample tube with a WHSV of 60,000 $mL \cdot h^{-1} \cdot g^{-1}$. The total height of the sample was about 20 mm which corresponds to the working height of the EPR cavity.

The *in situ* cw EPR spectra were recorded using the following typical settings: incident microwave power 75 mW, modulation frequency 100 kHz, modulation amplitude 0.4 mT. The external magnetic field was swept from 110 mT to 430 mT in 4096 steps. The total acquisition time of a single spectrum was 160 s. For time resolved cw EPR, spectra were continuously acquired using the rapid scan mode with 20 mT field sweep width centered at150 mT and 292

mT, respectively (modulation amplitude of 1.0 mT and incident microwave power of 15 mW). The acquisition time of an individual EPR spectrum was 1.5 s with the initial time synchronized within 1 s with the gas analytics.

The *ex situ* Q-band cw EPR measurements at room temperature were performed on a Bruker ESP 300 Q-band EPR spectrometer equipped with a ER 5106 QT cavity. Field modulation amplitude of 0.4 mT and an incident microwave power of 20 mW were used. Q-band pulse EPR measurements were performed using a Bruker ELEXSYS E580 EPR spectrometer equipped with a home-built TE011 microwave cavity.[29] W-band pulse EPR and ENDOR measurements were performed using a Bruker ELEXSYS E680 spectrometer operating at about 94 GHz in a home-built ENDOR microwave cavity.[30-32] (for details see SI Figures. S13,14)

3. RESULTS AND DISCUSSION

3.1 Materials characterization

For pure CeO_2 the flame-made powders were light yellow.[26] With increasing CuO content, they turned brown and eventually black. At a CuO content below 30 wt%, the XRD patterns correspond to pure CeO_2, and no patterns characteristic for CuO are detected (SI Figure S4, JCPDS No. 34-0394). This indicates that CuO is not doped inside the CeO_2 lattice, and that the majority of it likely forms surface amorphous species. In accordance with the XRD patterns, the TEM image only shows lattice fringes of cubic CeO_2 crystals for 20 wt% CuO-CeO_2 (Figure 1a). The primary particle size is ~5 nm. Both Ce and Cu are homogeneously distributed in the region corresponding to Figure 1b, as shown by the energy dispersive X-ray (EDX) spectroscopy (Figure 1c for Cu and d for Ce). The surface oxidation states of Cu and Ce are 2+ and 4+, respectively, as determined by XPS (SI Figure S5). Some Ce^{3+} were also detected on the surface. The size of the CeO_2 particles can be easily tuned by varying the ratio between the injection rate

of precursor solution and dispersion gas during pyrolysis (SI Table S1 and Figure S6). The redox properties of 20 wt% CuO-CeO_2 (5 ± 1 nm) and CuO were first studied by TPR (SI Figure S7). Pure CuO gives a maximum H_2 consumption at 433 K, which is, at least, 100 K lower than any other copper-containing catalyst.[33] In the present study the small particle size accounts for this low temperature reduction of CuO. The TPR signal of 20 wt% CuO-CeO_2 reveals a shoulder at 375 K and two peaks at 390 and 402 K, respectively. Reduction of CuO in CuO-CeO_2 proceeds accordingly already at much lower temperatures compared to pure CuO. The shoulder and peaks of the TPR curve for 20wt% CuO-CeO_2 indicate that the reduction process undergoes either with one copper species in multiple steps, or with multiple copper species in one/multiple steps. Note that pure CeO_2 cannot be reduced in this temperature range.[34] Again, the small particle size and homogeneous distribution of Cu lead to reduction peaks at least 40 K lower compared to CuO-CeO_2 materials that are prepared by other methods[33]. The molar ratio between the amount of consumed H_2 during TPR and the amount of Cu^{2+} present in the catalyst, as determined by atom emission spectroscopy, are 0.97 and 0.98 for CuO and 20 wt% CuO-CeO_2, respectively, indicating that most of the Cu^{2+} is reduced to Cu. Additional temperature programmed oxidation measurements (data not shown) revealed that these Cu^{+}/Cu^{0} species are readily reoxidized to Cu^{2+} in the presence of O_2 at room temperature. With such extraordinary redox properties at low temperature, the CuO-CeO_2 system is a perfect candidate for *in situ* EPR study, in which the changes of the Cu^{2+} species can be followed under oxidation and reduction condition.

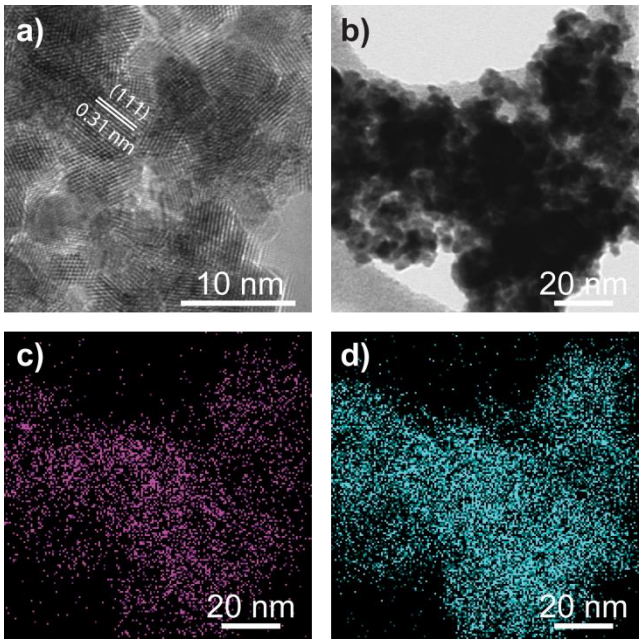

Figure 1. TEM images of 20 wt% CuO-CeO_2 at high (a) and low (b) magnifications. EDX element mapping of Cu (c) and Ce (d) corresponding to (b). Only the lattice fringe of CeO_2 is observed in TEM images. The lattice fringes correspond to the (111) planes. The distribution of Cu and Ce is homogeneous, as shown in the EDX element mapping.

Figure 2a shows the X-band cw EPR spectrum of CuO-CeO_2 (20 wt%) acquired at room temperature over a wide magnetic field range. The spectrum is composed of several narrow and broad signals. The comparison with previous studies[19,20,36] allows an analysis of Cu^{2+} (S = 1/2) in different states, namely isolated monomers, isolated dimers and amorphous clusters (or aggregates) of Cu^{2+} ions. Isolated Cu^{2+} ions give rise to narrow intense signals[19] around 325 mT (X-band). The additional features, resolved in the spectrum, are assigned to Cu^{2+} dimers and exhibit fine structure arising from interaction of the unpaired electrons of pairs of ferromagnetically coupled Cu^{2+} ions (S = 1). Each component of the fine structure comprises seven narrow lines (with relative intensities 1:2:3:4:3:2:1), resulting from coupling of the total electron spin to the two magnetic $^{63(65)}$Cu nuclei (natural abundance ^{63}Cu: 69.15%, ^{65}Cu: 30.85%, both I=3/2). The sharp lines in the range 120-180 mT are assigned to the "forbidden" $\Delta M_S=\pm 2$ transitions, which are characteristic for the triplet electron spin state of the dimer. The magnetic

parameters of the dimer ($g_{\perp}$=2.035, $g_{\parallel}$=2.216, $A_{\perp}(^{63}Cu)$ =1.3 mT, $A_{\parallel}(^{63}Cu)$ =9.1 mT, D = 69.1 mT) obtained from the numerical simulation of the experimental EPR spectrum are in good agreement with previously reported values[19] (see also SI, Figure S8). Due to the well-defined EPR spectrum, Cu^{2+} dimers represent perfect candidates for probing of the redox behavior of the catalysts in the *in situ* study. The well pronounced monomer and dimer signals are superimposed with a broad signal contribution that is attributed to the Cu^{2+} ions present in the form of amorphous aggregates. The broad linewidth indicates that they are affected by strong dipolar interactions between paramagnetic ions and/or by ferromagnetic couplings.[20] The contributions from the signals of aggregates, dimers and monomers to the EPR spectrum are estimated to be about 85-90%, 10-15% and <5%, respectively.

The assignment of the X-band EPR signals is supported by analysis of the Q-band cw EPR spectrum (Figure 2b) which is in qualitative agreement with a previously reported one.[19] In order to get additional insight into the nature of the aggregates, a microwave nutation EPR experiment was performed at Q-band frequency (see SI Electron-spin nutation experiment). This provides information on the spin state(s) of the individual spectral contribution. Comparison of the nutation frequency of the broad EPR signal contribution with the dimer (S = 1) yielded the average aggregate spin state $S \approx 2$. Thus, the aggregates contain on average four Cu^{2+} atoms with ferromagnetically coupled unpaired electrons. Unpaired electrons with antiferromagnetic coupling are EPR silent.

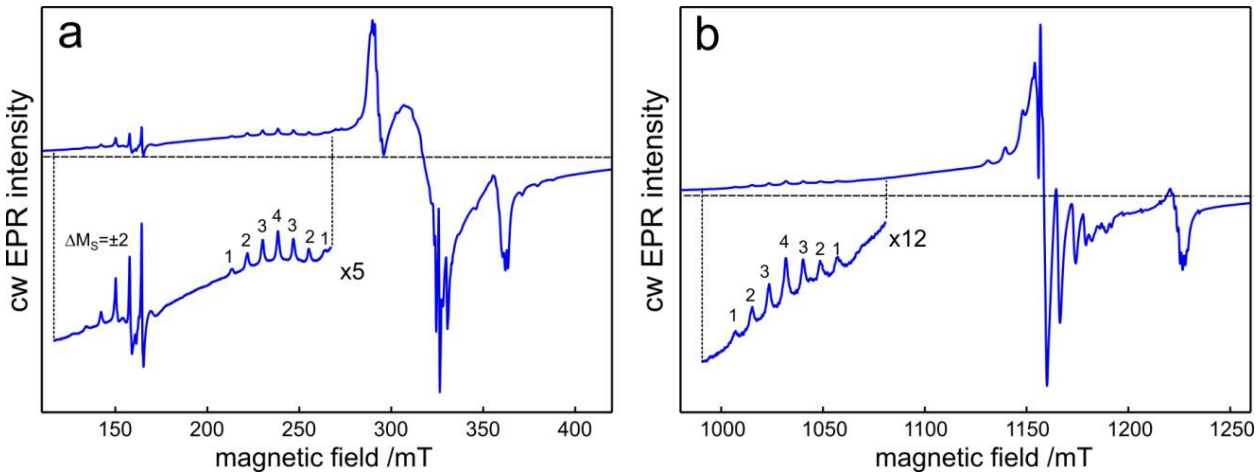

Figure 2. (a) cw X-band (9.33 GHz) and (b) Q-band (33.93 GHz) EPR spectra of 20 wt% CuO-CeO_2 under air acquired at room temperature.

3.2 Reduction and reoxidation mechanisms

Under air or N_2 the EPR spectrum of 20 wt% CuO-CeO_2 does not reveal substantial changes in the temperature range between 293 K and 473 K. However, exposure to a flow of 1% CO (balance N_2) at 453 K leads to a decrease of all EPR signal intensities, i.e. monomer, dimer, and aggregates (Figure 3a), indicating the reduction of all three species upon exposure of the catalyst to CO. After ten minutes of CO treatment the monomer and dimer signal intensities fell below 5% of their initial values. However, a substantial part of the broad signal contribution still remains even after 30 min exposure to CO. Thus, a certain amount of Cu^{2+} aggregates is present in the material that cannot be reduced under present reaction conditions and still contributes to the remaining signal. Subsequent to the CO exposure the reactor was purged with a flow of pure N_2 at 453 K for 140 min in order to remove any reductive gas. Interestingly, a slow increase of all three spectral contributions is observed in pure N_2, indicative for a partial reoxidation of Cu^{+}/Cu^{0} to Cu^{2+} in spite of the absence of oxygen in the gas phase (Figure 3a). This partial reoxidation of Cu^{+}/Cu^{0} will be discussed in detail below.

After the catalyst had subsequently been exposed to 1% O_2 gas, all signal intensities were restored to the initial value, indicating full reoxidation of Cu^{+}/Cu^{0} and the reversibility of the redox cycle. The results from time resolved experiments during such reduction/reoxidation processes are presented in Figure 3b, showing the intensity of the Cu^{2+} dimer peak (270-290 mT, see insert Fig. 3a) as a function of time, together with the analytic results of the gas composition. Here it can be seen that the EPR intensity of Cu^{2+} species decreases in two steps under 1% CO. First a fast reduction of ~90% of the Cu^{2+} dimers is observed, followed by a very slow reduction of the remaining Cu^{2+} (Note: TPR experiments showed that pure Ce^{4+} cannot be reduced at 453 K). Simultaneously only CO_2 and no CO is detected in the initial period, until ~90% of the Cu^{2+} dimers have been reduced, demonstrating the full conversion of all incoming CO to CO_2. Only after the majority of the Cu^{2+} species is reduced CO can be detected in the outlet gas flow. Moreover, the shoulders in the CO_2 concentration profile as a function of time indicate a multistep reduction process, where individual steps proceed with different reaction rates. In agreement with the first step in both of the above described redox mechanisms (*synergetic* and *direct mechanism*, see eq. 1) one can assume following reactions to take place upon exposure of the fully oxidized CuO-CeO_2 catalyst to CO:

$$(CuO)_2 + CO \rightarrow Cu_2^{+}O^{2-} + CO_2 \text{ and / or } (CuO)_2 + 2CO \rightarrow 2Cu^{0} + 2CO_2$$

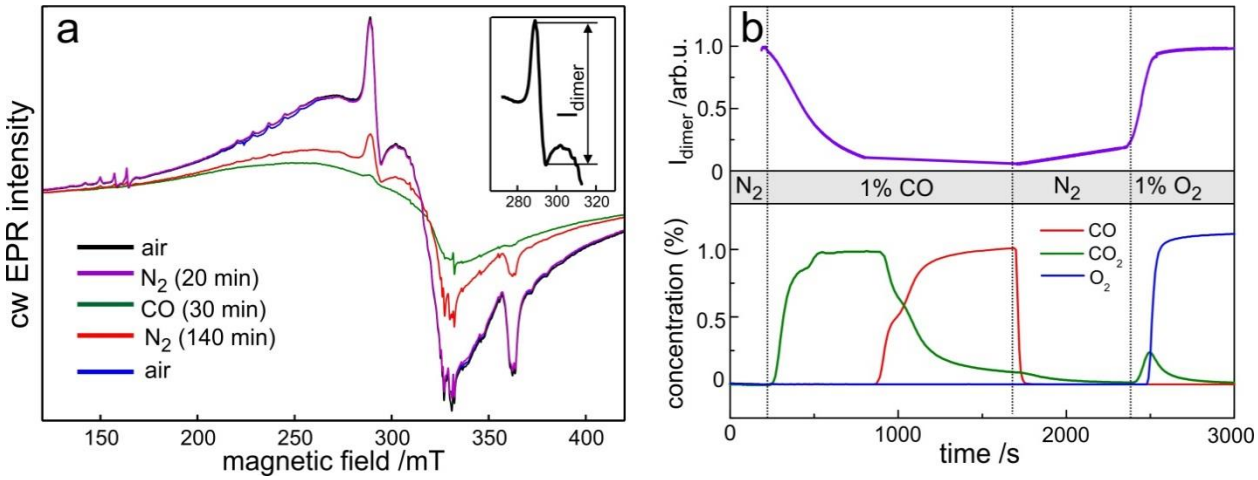

Figure 3. (a) X-band cw EPR spectra of 20 wt% CuO-CeO_2 recorded at 453 K during the treatment with air/N_2/CO/N_2/air. The durations of the particular gas treatments are indicated. The insert shows the dimer EPR signal used for kinetic measurements. (b) Upper trace: Time dependence of Cu^{2+} dimer EPR signal intensity at 289 mT during the N_2/CO/N_2/air cycle at 453 K. Lower traces: Corresponding CO, CO_2 and O_2 concentration simultaneously recorded by the gas analysis system.

Regarding the subsequent slow increase of EPR intensity of all Cu^{2+} species in pure N_2 described above, this has to originate from a reoxidation of previously reduced Cu species (Cu^{+} and/or Cu^{0}) by CeO_2. Since a reoxidation by O_2 impurities in the gas system can be excluded (nitrogen gas was purified using an oxygen trap BOT-2 from Agilent with an O_2 outlet concentration of less than 1 ppb), CeO_2 represents the only remaining species capable to oxidize Cu^0/Cu^+ under these conditions, according to $Cu^{+} + Ce^{4+} \rightarrow Cu^{2+} + Ce^{3+}$ and/or $Cu^{0} + 2Ce^{4+} \rightarrow Cu^{2+} + 2Ce^{3+}$ reaction pathways. In order to determine the resulting oxidation state of Cu and Ce on the surface of the reduced sample, the CO pretreated sample was cooled from 453 K to room temperature under CO. Subsequently, CO was replaced by a nitrogen flow and the sample was kept under N_2 flow for 15 hours. The result of such N_2 treatment at room temperature differs from that at 453 K, and indicates a surface passivation of the sample. The EPR spectrum shows that the sample remains in the "reduced" form and does not exhibit major changes even in the presence of air for several hours (SI Figure S9). An XPS spectrum of the

sample revealed that predominantly Cu^{+} is present on the surface (SI Figure S10b). The Ce^{3+} content is also higher than that in the fresh catalysts (SI Figure S10a), suggesting the formation of Ce^{3+}. The corresponding XRD, however, showed reflections of Cu metal nanoparticles and Cu_2O (SI Figure S11). Such change in XRD pattern is in agreement with a previous report.[13] The surface of the Cu nanoparticles is obviously oxidized to Cu_2O, and since XPS is surface sensitive to only the first layers, no metallic Cu^0 signal is observed in XPS. EPR spectra showed a slow increase of Cu^{2+} under N_2 flow. However, the Cu^{2+} was also not detected by XPS, indicating that the newly formed Cu^{2+} species are not on the surface. This also suggests a redox process inside the solid catalyst. Due to the low concentration of the Cu^{2+} species and the possibility that the copper species not forming a coherent phase are being amorphous, they are not observed in the XRD. The oxidation state of Cu and Ce under CO and N_2 conditions was confirmed by XANES. After 200h of operation under the PROX conditions, the CuO-CeO_2 (20wt%CuO) catalyst was found to be predominantly in the oxidized form (Cu^{2+} and Ce^{4+}) with only 5.2% of Ce in the 3+ state (Figure 4ab blue curve and Figure S12a). After 1 h CO treatment and subsequent exposure to N_2 at 473 K, the majority of Cu^{2+} was converted to Cu and the content of Ce^{3+} increased to 13.1% (Figure 4ab red curve and Figure S12b). Thus, the reduction of Cu^{2+} by CO and reduction of Ce^{4+} by Cu takes place. We note that pure CeO_2 TPR data do not show any reduction at 473 K, suggesting that Ce^{4+} is possibly reduced by Cu or Cu^{+}. When the catalyst was kept under CO for 12 h at 473 K, the content of the Ce^{3+} increased to 15.7% (Figure 4b black curve and Figure S12c), showing further reduction of the catalysts. The *in situ* EPR spectra, *ex situ* XPS, XANES and XRD patterns clearly support a reoxidation step $Cu^{+} + Ce^{4+} \rightarrow Cu^{2+} + Ce^{3+}$ and/or $Cu + 2Ce^{4+} \rightarrow Cu^{2+} + 2Ce^{3+}$ for all the copper species (monomers, dimers and aggregates), corresponding to the *synergetic mechanism*. After pure N_2 is replaced with 1% O_2 at 453 K,

Cu^0/Cu^+ is quickly oxidized into Cu^{2+}. This is also in agreement with XRD results, which show no reflections for Cu^0 metal nanoparticles and Cu_2O (SI Figure S11) after O_2 treatment. Thus, O_2 shifts the reaction of $2Ce^{3+} + ½O_2 \rightarrow 2Ce^{4+} + O^{2-}$ towards the right rapidly, and also increases the reaction rate of $Cu^+ + Ce^{4+} \rightarrow Cu^{2+} + Ce^{3+}$ and/or $Cu^0 + 2Ce^{4+} \rightarrow Cu^{2+} + 2Ce^{3+}$. Another possible explanation is that O_2 directly reacts with Cu^+/Cu^0. Therefore, at this stage, the possibility of participation of the *direct mechanism* cannot be excluded.

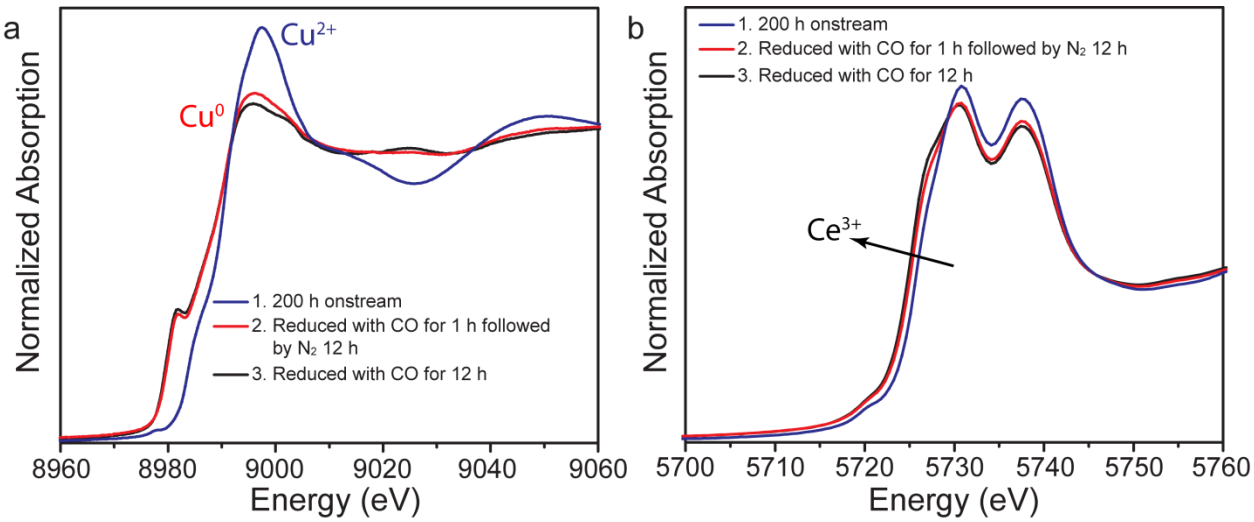

Figure 4. (a) Cu K-edge XANES and (b) Ce L_3-edge XANES of $CuO\text{-}CeO_2$ (20wt%CuO) catalysts recorded after different pretreatment conditions. All samples were transferred into an airtight chamber in the glove box to prevent exposure to air or oxygen. Sample 1 (blue curve): The catalyst was used for PROX reaction at 387 K for 200 h. Sample 2 (red curve): sample 1 was reduced by CO at 473 K for 1 h, and then subsequently treated with N_2 at the same temperature for 12 h. Sample 3 (black curve): sample 1 was reduced by CO at 473 K for 12 h.

While both gas phase O_2 and lattice O^{2-} are involved in the *synergetic mechanism*, the lattice O^{2-} should not participate in the *direct* one. Such difference can be probed using isotope enriched oxygen gas. The isotope substitution should occur predominantly at O–Ce in the *synergetic mechanism* and exclusively at O–Cu in the *direct mechanism* (Figure 5a,b).

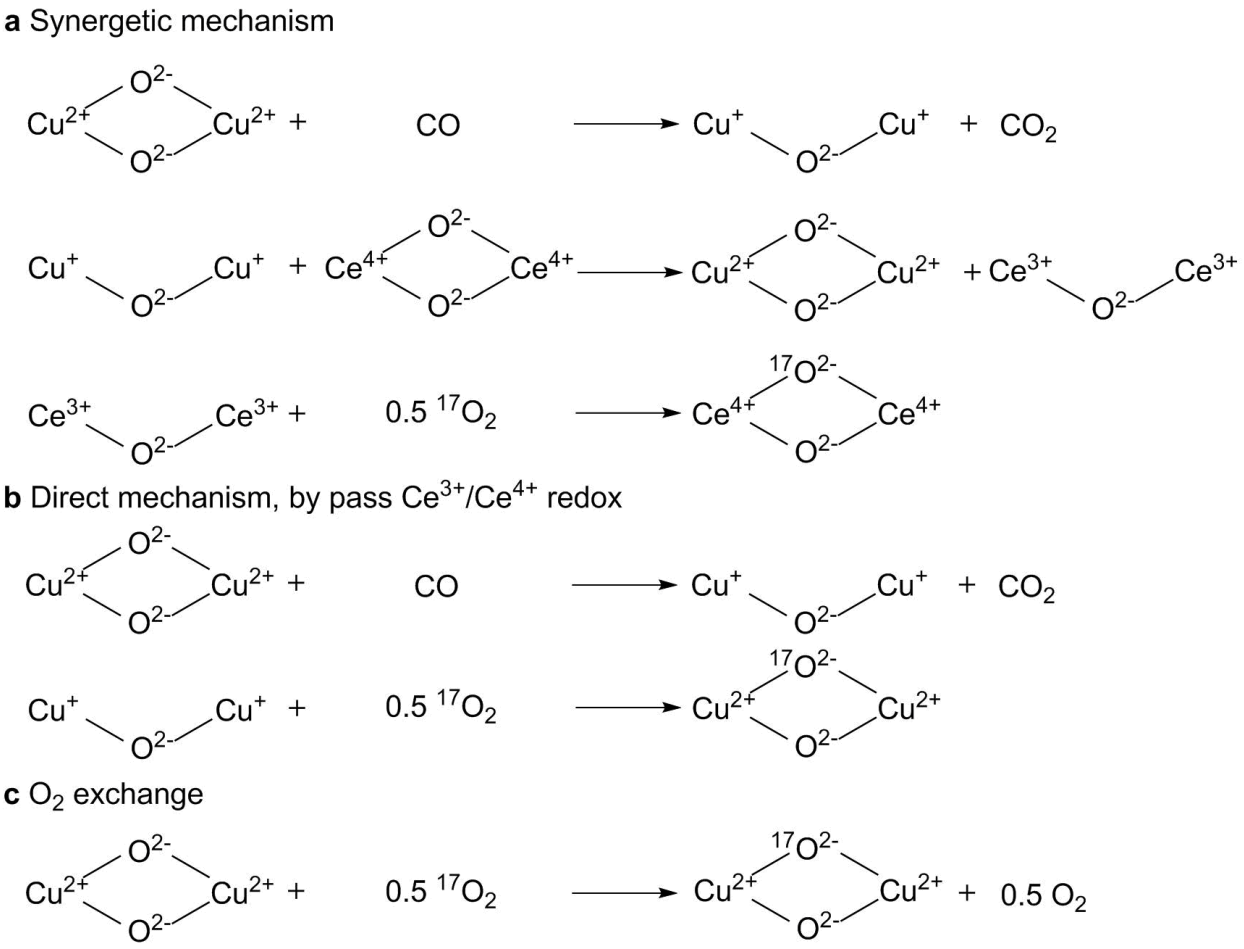

Figure 5. Reaction schemes demonstrating the elucidation of the reaction mechanism using isotopically enriched oxygen ($^{17}O_2$) for (a) the synergetic mechanism. (b) the direct mechanism. (c) O_2 exchange reaction.

EPR enables the monitoring of ^{17}O exchange in Cu^{2+} dimers during reduction/reoxidation cycles (Figure 6). The reconstitution of the dimers by ^{17}O leads to significant changes in their EPR spectra. The replacement of nonmagnetic ^{16}O (nuclear spin I = 0) by ^{17}O results in hyperfine interactions of unpaired electrons with the magnetic ^{17}O nuclei (I = 5/2). In contrast to the strong Cu hyperfine interaction, which is directly observable in the EPR spectrum of Cu^{2+} dimers, the smaller ^{17}O hyperfine interaction in combination with the high nuclear spin of ^{17}O (I = 5/2) results predominantly in EPR line broadening of the dimer signal. Figure 6a shows EPR spectra of a fully ^{16}O oxidized sample and that after three $N_2/CO/N_2/^{17}O_2$ cycles performed at

453 K. After $^{17}O_2$ reoxidation, the EPR spectral contributions of Cu-dimers and monomers undergo changes (Figure 6a and Figure S21). The direct detection of ^{17}O broadening is impossible in cw EPR spectrum of the aggregates due to the large intrinsic EPR linewidth. Comparison of the EPR spectra at half-field and in the region between 200-275 mT (with resolved dimer $A_{\|}$ splitting) reveals larger spectral changes at half-field after the $^{16}O_2$ and $^{17}O_2$ treatments, see insert in Figure 6a. This is because the line broadening due to unresolved ^{17}O hyperfine couplings is more pronounced in this spectral region owing to the smaller intrinsic EPR linewidth. Figure 6b depicts the EPR spectra in the half-field region after correction for the spectral contribution due to Cu-aggregates. The spectrum of the ^{17}O treated sample can be deconvoluted in two contributions, resulting from dimer fractions with and without coupled ^{17}O-nuclei (one or two) with approximately equal weights. The subtraction of the normalized ^{16}O-dimer spectrum from the spectrum of the ^{17}O treated sample reveals the spectral contribution of the dimer fraction containing the ^{17}O-nuclei (red trace in Figure 6b). This contribution is well described by the ^{16}O half-field EPR spectrum convoluted with a gaussian line, Figure 6b. The width of this line (FWHH = 3.5mT) is consistent with substantial Cu^{2+}-^{17}O hyperfine coupling, as for instance, determined for a $[Cu\,(H_2{}^{17}O)_6]^{2+}$ complex.[37] The very large broadening of the half-field lines due to the ^{17}O hyperfine interaction allows for an exact quantification of the remaining dimer fraction that exclusively contains ^{16}O nuclei. The peak-peak intensity of the largest half-field line around 165 mT is used for this purpose (Figure 6a). The weights of single and double ^{17}O reconstituted dimer fractions cannot be elucidated separately.

One has to consider, however, that the presence of Cu^{2+}-^{17}O species could also originate from oxygen exchange between O_2 in the gas phase and O^{2-} at the surface (see Figure 5c). In order to check for a possible oxygen exchange between the gas phase and the catalyst, multi-pulse TAP

experiments were performed. The freshly calcined and, hence, fully oxidized ^{16}O-catalyst was exposed to sequences of $^{18}O_2$ oxygen pulses at 393 K and 473 K ($^{18}O_2$ is used here to reduce the cost of the experiment). The results clearly demonstrate that there is no oxygen exchange between $^{18}O_2$ in the gas phase and ^{16}O in the CuO-CeO_2 composite (SI Figure S13).

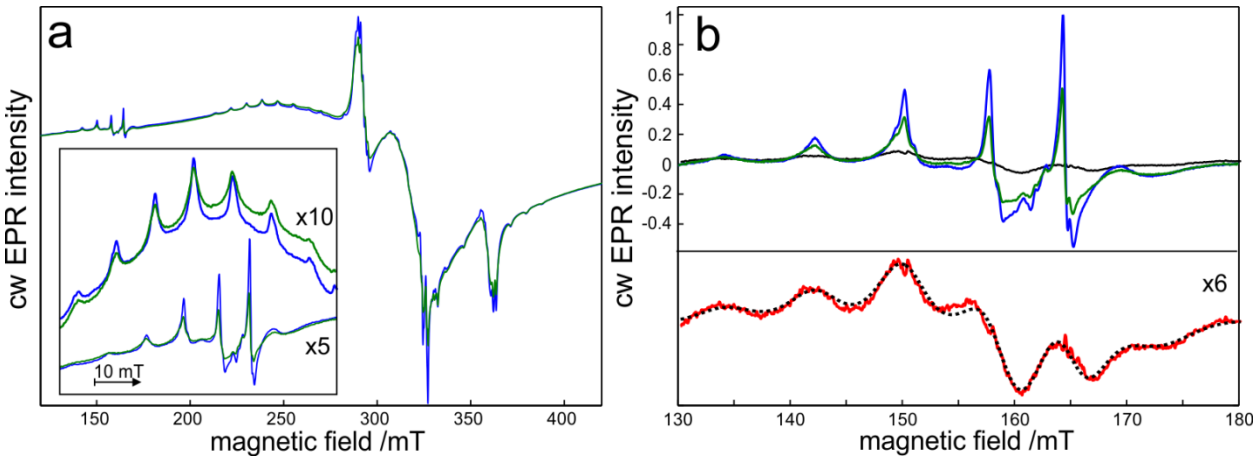

Figure 6. (a) X-band cw EPR spectra of 20 wt% CuO-CeO_2 after treatment with $N_2/CO/N_2/^{16}O_2$ (blue line) and $N_2/CO/N_2/^{17}O_2$ (green line) cycles recorded at 293 K. (b) Baseline corrected half-field region ($\Delta M_S=\pm2$) of spectra from (a). The red line shows the spectral contribution of the fraction of the Cu^{2+} dimers containing ^{17}O. The EPR signal of the ^{16}O treated sample convoluted with a Gaussian function with 3.5 mT width (FWHH) is shown as dashed line.

Figure 7a shows the EPR spectra in the half-field dimer region recorded after multiple CO-reduction/$^{17}O_2$-oxidation cycles at 453 K starting with pure ^{16}O containing 20 wt% CuO-CeO_2 composite. After the first $^{17}O_2$ reoxidation treatment the EPR signal intensity of $Cu_2{}^{16}O_2$ dimers is reduced by 20% which means that 20% of the dimers are ^{17}O reconstituted, i.e. $Cu_2{}^{17}O_2$ or $Cu_2{}^{16}O{}^{17}O$ are formed. The subsequent sample treatments further reduce the amount of exclusively ^{16}O containing dimers to 61% and 47% at the second and third $^{17}O_2$ cycles, see Figure 7a. Noteworthy, this process is completely reversible. After several CO-reduction/$^{16}O_2$-oxidation cycles of the ^{17}O pretreated sample the original signal intensities of the ^{16}O sample are

restored stepwise, see Figure 7b. The possibility to quantify the oxygen replacement in the dimers allows a discussion of the catalyst's redox mechanisms. In the case of only the *direct mechanism* acting, the Cu-dimers should be oxidized by ^{17}O and already after one $CO/N_2/^{17}O_2$ sample treatment the major fraction of the dimers should contain at least one ^{17}O atom in the bridge, resulting in a complete broadening of half-field EPR signals. This is, however, not the case, see Figure 7a. After one exchange, only 20% of the oxygen species are replaced by ^{17}O, while 80% still contain ^{16}O in both bridges. This suggests that the relative contribution of the direct and the indirect pathways approximately corresponds to this ratio, for more details see SI (Contributions of the *synergetic* and the *direct* mechanism in the redox process).

The predominant replacement of ^{16}O by ^{17}O in the CeO_2 framework was additionally confirmed by W-band ENDOR (electron-nuclear double resonance) experiments. A strong ^{17}O-signal of weakly coupled nuclei was detected in the sample which had been treated to reconstitute only 50% of dimers by ^{17}O (SI, W-band ENDOR experiment). This shows the large concentration of non-bridging ^{17}O in the vicinity of reoxidized dimers.

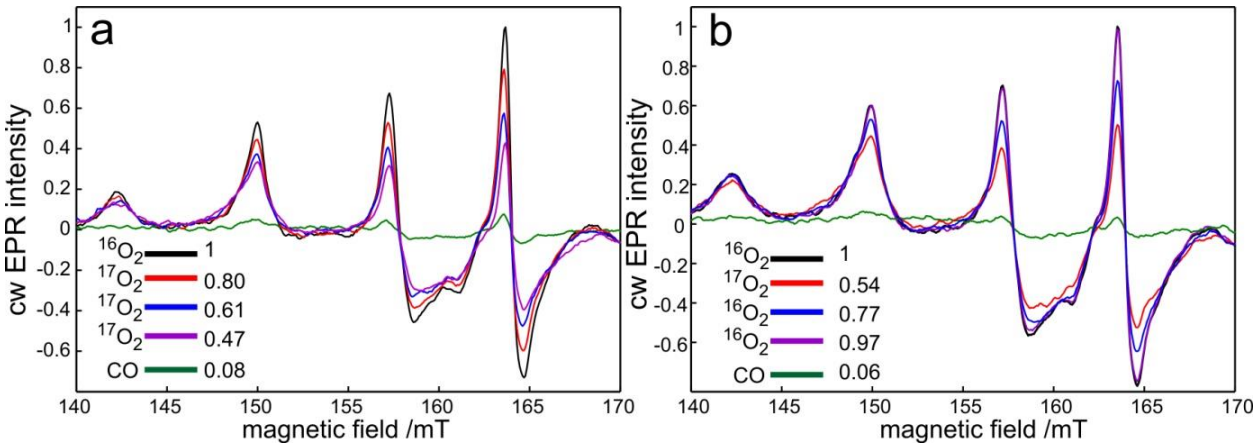

Figure 7. Half-field region EPR signals of 20 wt% $CuO\text{-}CeO_2$ recorded at 453 K after treatment with $N_2/CO/N_2/O_2$ cycles using $^{16}O_2$ and $^{17}O_2$. Development of EPR signals during (a) ^{16}O -> ^{17}O and (b) ^{17}O ->^{16}O cycles. The different O_2 isotopes used in each cycle are indicated in the legend

as $^{16}O_2$ or $^{17}O_2$. The number behind the legend bar is the relative concentration of exclusively ^{16}O containing dimers, e.g. 1 means the concentration of exclusively ^{16}O containing dimers is 100%.

In situ EPR in combination with oxygen isotope substitution was also used under CO oxidation conditions. In the first step, the freshly ^{17}O reconstituted sample was exposed to a gas mixture of CO 1.6% and $^{16}O_2$ 1.7% at 298 K (WHSV = 60,000 $mL \cdot h^{-1} \cdot g^{-1}$) under which CO conversion of 1% was measured. After 30 minutes no changes in the dimer half-field EPR signal were detected. Subsequently, the sample was heated to 443 K, and treated by the same gas mixture for 30 min. At this temperature 100% of CO was converted to CO_2. The sample was cooled down to 298 K and its EPR spectrum was compared to the initial one (Figure S22). In contrast to CO-reduction/O_2-reoxidation cycles no replacement of ^{17}O in the Cu-dimer bridge was found during the catalytic CO conversion, i.e. the half-field EPR signal did not show any changes. This suggests that the Cu^{2+}-dimers do not play a major role for CO conversion at 443 K. Thus Cu monomers and aggregates are the possible active species for CO oxidation in excess amount of O_2. It has also been reported that Cu^+, which could not be observed by EPR, may be the active species in CO oxidation[9].

3.3 Catalytic activity

In order to investigate the relevance of the above findings under reaction conditions, the PROX in hydrogen-rich gas[38] on the 20wt% CuO-CeO_2 catalyst has been studied. This reaction is particularly important for the purification of H_2-rich gas feed in low-temperature fuel cells, for which CO concentrations lower than 100 ppm are required. Note that besides its activity for CO oxidation, here also the catalyst's selectivity towards CO oxidation has to be considered. While at best almost all CO is oxidized to CO_2, there should be as little oxidation of excess H_2 as possible. EPR spectra were recorded *in situ* during the catalyst's exposure to a continuous flow of a gas mixture containing 1 vol% CO, 1 vol% O_2, 50 vol% H_2 and 48 vol% N_2. At low

temperatures (< 389 K, Figure 8), the catalyst was active for CO oxidation only, with CO conversion increasing from 18% to 96% as the temperature was raised from 328 K to 389 K. Accordingly, selectivity is always 100% in this temperature range. Furthermore, no changes of the EPR signals of all three Cu^{2+} species (monomers, dimers, aggregates) were detected. For higher temperatures, in contrast, all CO is oxidized to CO_2 (100% CO conversion) and the selectivity started to decrease due to the onset of the simultaneous H_2 oxidation. Upon increasing the temperature from 389 K to 423 K the selectivity decreases from 100% to 50%. Despite these changes in the catalytic performance, the EPR signals were still unchanged and, hence, all Cu species were still in the Cu^{2+} state up to 408 K under PROX reaction conditions (Figure 8 red to purple). Most easily this may be explained by the fact, that under these conditions (selectivity higher 50%) oxygen in the inlet gas (1 vol% O_2) was not yet consumed completely. Accordingly, the presence of O_2 in the gas phase kept the Cu species in their highly oxidized state (Cu^{2+}). Above 423 K, however, O_2 was completely consumed, corresponding to selectivities of 50% and lower, and the Cu^{2+} species were reduced by CO and H_2 in the gas mixture (Figure 8 cyan to green). Subsequent exposure of the sample to air led to the initial state of the catalyst, and all Cu^{2+} EPR signals completely recovered.

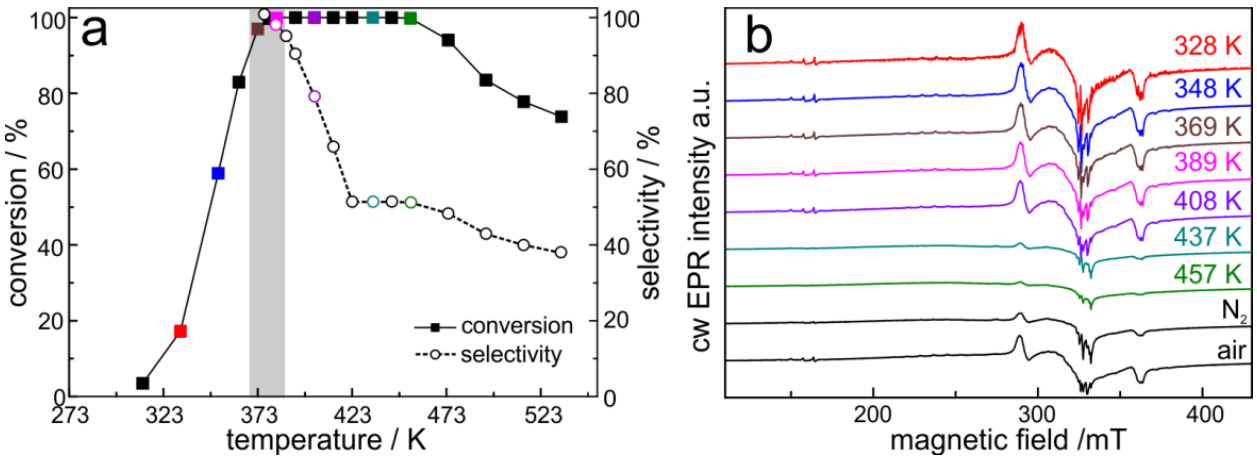

Figure 8. (a) Conversion and selectivity of CO as a function of temperature for PROX. The conversion reaches its maximum (> 99%) at 389 K, and remains above 99% until 457 K. The selectivity remains at 100% up to 389 K and drops to 50 % at 423 K. Catalyst: 20wt% CuO-CeO_2, particle size 5 ± 1 nm. (b) *In situ* EPR spectra of 20wt% CuO-CeO_2 at different temperature in the PROX reaction. Each spectrum is correlated to the conversion and selectivity point with the same color code in (a).

The above described *in situ* EPR studies during the alternating exposure of the catalyst to CO and O_2 showed that the redox reactions in the investigated CuO–CeO_2 system proceed simultaneously via the *synergetic* and the *direct mechanism*, with the *synergetic mechanism* being dominant. Since both CuO and CeO_2 participate in the *synergetic mechanism*, strong interactions between the two oxides should be crucial for high activities in any related catalysis. Such interactions require a large interface between CuO and CeO_2, which can be achieved by optimizing either the CuO content or the CuO–CeO_2 particle size. In the following we explored the influence of both parameters on the catalyst's activity in order to further optimize the CuO–CeO_2 catalyst for the PROX reaction.

First the CuO content was varied between 1 wt% and 40 wt% while the size of the CuO–CeO_2 particles remained constant at 5 ± 1 nm. Increasing the CuO content from 1 wt% to 20 wt% results in a significantly improved activity for CO oxidation over the whole temperature range investigated (Figure 9a). A further increase to 40 wt% CuO, however, resulted again in lower activities, which are close to the values obtained with the 1 wt% CuO-CeO_2 catalyst. Moreover, the catalyst with the optimal content of 20 wt% CuO also shows the widest operation window of 11 K, which is defined as the temperature range in which both conversion and selectivity exceed 99%. For a more detailed comparison of all catalysts with different CuO contents we refer the reader to the SI (SI, Figure S18). From these results we assume that with increasing CuO content, up to 20 wt%, a larger Cu-Ce interface is created. For even higher CuO contents, however, the

amount of Ce^{4+} becomes limiting, and eventually results in an overall smaller CuO–CeO_2 interface. Since the CuO–CeO_2 interface is a key factor for the *synergetic mechanism*, the decreasing activity with increasing loading for high CuO contents (<40 wt%) also indicates that the *synergetic mechanism* is dominant, in agreement with the above described findings

Next we varied the size of the CuO–CeO_2 particles, while keeping the Cu loading constant at 20 wt%. As the particle sizes are increased, the amount of surface Cu^{2+} species will decrease due to the decrease of surface area. As a result, such an increase of the size of CuO-CeO_2 particles, from 5 ± 1 to 30 ± 4 nm, resulted in much lower activities for CO oxidation (Figure 9b). The selectivity for CO oxidation, on the other hand, increases at the same time as the CuO particle size increases. Due to the more pronounced changes in activity, however, this results in a significant decrease of the operation window (Figure 9b). So far, the 11 K operation window with at least 99% CO conversion and 99% selectivity, obtained for the catalyst with 5 ± 1 nm CuO nanoparticles and 20 wt% CuO content, is among the highest value reported using any catalysts[38,39] at similar conditions. In addition, the optimized catalyst can be used at high space velocity (600,000 $mL \cdot h^{-1} \cdot g^{-1}$) while a complete removal of the CO is still achieved (Figure S19).

Finally, we also determined the long term stability of the 20 wt% CuO-CeO_2 catalyst since this is an important parameter for practical applications. These measurements have been performed under two different sets of flow rates. Running the reaction at 387 K and with a flow of 600,000 $mL \cdot h^{-1} \cdot g^{-1}$ (1% CO, 1% O_2, H_2, N_2) 52% CO conversion and 100% selectivity are achieved, and no changes have been observed for at least 100 h of operation (Figure S20). This high stability of the catalyst was additionally tested under real operation conditions, in which 100% conversion

and 100% selectivity are obtained (at 387 K and with a flow of 60,000 mL·h^{-1}·g^{-1}). Even under these conditions a stable performance was achieved for at least 193 h of operation.

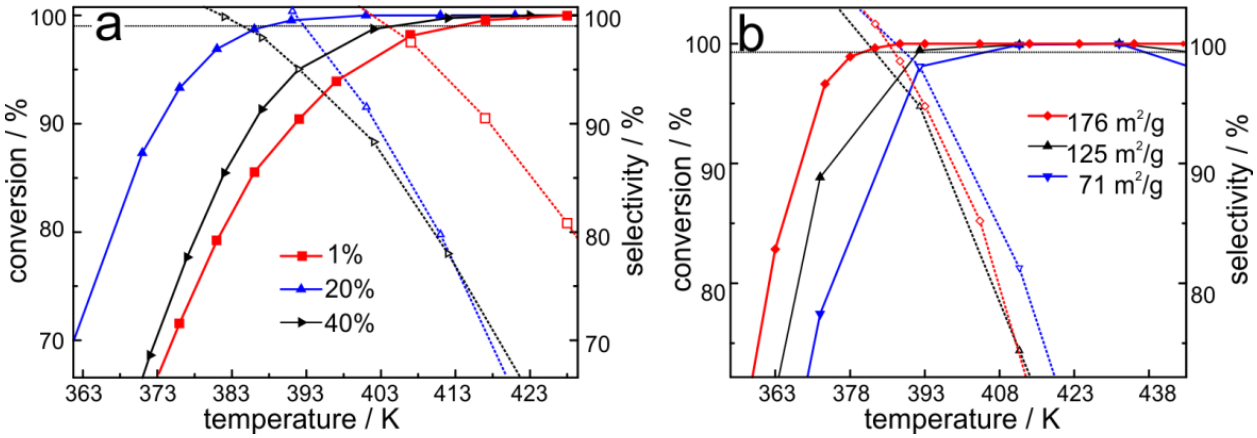

Figure 9: PROX conversion (solid line) and selectivity (dashed line). The horizontal dotted line represents 99% conversion and selectivity. WHSV = 60,000 mL·h^{-1}·g^{-1}. (a) Conversion and selectivity as a function of temperature for PROX over catalysts with different CuO wt% content. (b) Conversion and selectivity as a function of temperature for PROX for catalysts with different sizes.

4. CONCLUSION

In situ EPR, in conjunction with online gas analysis and TAP studies, provided a detailed insight into the redox mechanism of CuO-CeO_2 catalysts. Combination of EPR spectroscopy with gas analysis enabled the identification of the *synergetic mechanism* as the major redox reaction pathway. $^{17}O_2$ isotopic labeling experiments additionally revealed the participation of another co-existing mechanism, the *direct mechanism*, which only involves Cu species and bypasses Ce^{4+}/Ce^{3+}. For optimal redox catalysts based on this system, the interaction and interface between Cu and Ce should be maximized. For instance, in the application of the system in PROX, the best catalyst was found to contain 20 wt% CuO and to have CuO–CeO_2 particle sizes of 5 ± 1 nm, resulting in a temperature operation window of 11 degrees from 377 K to 388 K. *In situ* EPR spectroscopy[40,41], in particular using time dependent EPR experiments, can be a powerful

tool in catalysis research, as, for instance, also repeatedly shown by Brückner and colleagues[42]. We plan to extend the application of this methodology to other reactions, such as the water gas shift reaction and the selective catalytic reduction of nitric oxide. It is foreseen that *in situ* EPR could help to unveil the relationship between electronic structure and catalytic property of the true active species in these reactions.

Acknowledgments

This work was conducted in the framework of the ERC Advanced Grant projects "POLYCAT" and "FLAMENANOMANUFACTURE" and the Seventh Framework Program (FP7/2007-2013) (grant agreement no. 247283). We greatly acknowledge the support of this research by the Alexander von Humboldt-Stiftung and Max Planck Society. We thank the B18 Beamline in Diamond Light Source, the SP10306 UK Catalysis Hub BAG proposal, Dr. Peter Wells and Mr. Liqun Kang for the XANES measurement and analysis. We thank Claudia Weidenthaler and Olga Petrova for helping us with the analysis of the XPS data and Angelika Brückner for valuable discussion concerning *in situ* EPR.

Supporting Information Available: The digital picture and illustration of the *in situ* EPR setup, the flame spray pyrolysis setup, XRD, XPS, XANES, TPD data, TEM images of CuO_2-CeO_2 with different particle sizes, the oxygen exchange experiment, the electron-spin nutation experiment, the W-band ENDOR experiment and the PROX results. This material is available free of charge via the Internet at http://pubs.acs.org.

References

(1) Trovarelli, A. *Catal. Rev.* **1996**, *38*, 439.
(2) Liu, W.; Flytzani-Stephanopoulos, M. *J. Catal.* **1995**, *153*, 304.

(3) Martinez-Arias, A.; Fernandez-Garcia, M.; Galvez, O.; Coronado, J. M.; Anderson, J. A.; Conesa, J. C.; Soria, J.; Munuera, G. *J. Catal.* **2000**, *195*, 207.

(4) Kaspar, J.; Fornasiero, P.; Graziani, M. *Catal. Today* **1999**, *50*, 285.

(5) Herman, R. G.; Klier, K.; Simmons, G. W.; Finn, B. P.; Bulko, J. B.; Kobylinski, T. P. *J. Catal.* **1979**, *56*, 407.

(6) Grunwaldt, J. D.; Molenbroek, A. M.; Topsoe, N. Y.; Topsoe, H.; Clausen, B. S. *J. Catal.* **2000**, *194*, 452.

(7) Tschope, A.; Liu, W.; Flytzani-Stephanopoulos, M.; Ying, J. Y. *J. Catal.* **1995**, *157*, 42.

(8) Sedmak, G.; Hocevar, S.; Levec, J. *J. Catal.* **2003**, *213*, 135.

(9) Liu, Y.; Fu, Q.; Flytzani-Stephanopoulos, M. *Catal. Today* **2004**, *93-5*, 241.

(10) Graciani, J.; Mudiyanselage, K.; Xu, F.; Baber, A. E.; Evans, J.; Senanayake, S. D.; Stacchiola, D. J.; Liu, P.; Hrbek, J.; Sanz, J. F.; Rodriguez, J. A. *Science* **2014**, *345*, 546.

(11) Skarman, B.; Grandjean, D.; Benfield, R. E.; Hinz, A.; Andersson, A.; Wallenberg, L. R. *J. Catal.* **2002**, *211*, 119.

(12) Wang, X. Q.; Rodriguez, J. A.; Hanson, J. C.; Gamarra, D.; Martinez-Arias, A.; Fernandez-Garcia, M. *J. Phys. Chem. B* **2006**, *110*, 428.

(13) Ciston, J.; Si, R.; Rodriguez, J. A.; Hanson, J. C.; Martinez-Arias, A.; Fernandez-Garcia, M.; Zhu, Y. M. *J. Phys. Chem. C* **2011**, *115*, 13851.

(14) Mudiyanselage, K.; Senanayake, S. D.; Feria, L.; Kundu, S.; Baber, A. E.; Graciani, J.; Vidal, A. B.; Agnoli, S.; Evans, J.; Chang, R.; Axnanda, S.; Liu, Z.; Sanz, J. F.; Liu, P.; Rodriguez, J. A.; Stacchiola, D. J. *Angew. Chem. Int. Ed.* **2013**, *52*, 5101.

(15) Shi, J. L. *Chem. Rev.* **2013**, *113*, 2139.

(16) Il'ichev, A. N.; Firsova, A. A.; Korchak, V. N. *Kinet. Catal.* **2006**, *47*, 585.

(17) Moreno, M.; Bergamini, L.; Baronetti, G. T.; Laborde, M. A.; Marino, F. J. *Int. J. Hydrogen Energ.* **2010**, *35*, 5918.

(18) Aboukais, A.; Bennani, A.; Aissi, C. F.; Guelton, M.; Vedrine, J. C. *Chem. Mater.* **1992**, *4*, 977.

(19) Aboukais, A.; Bennani, A.; Aissi, C. F.; Wrobel, G.; Guelton, M.; Vedrine, J. C. *J. Chem. Soc. Faraday T.* **1992**, *88*, 615.

(20) Soria, J.; Conesa, J. C.; Martinezarias, A.; Coronado, J. M. *Solid State Ion.* **1993**, *63-5*, 755.

(21) Aboukais, A.; Bennani, A.; LamonierDulongpont, C.; AbiAad, E.; Wrobel, G. *Colloids Surf., A* **1996**, *115*, 171.

(22) Kydd, R.; Teoh, W. Y.; Wong, K.; Wang, Y.; Scott, J.; Zeng, Q. H.; Yu, A. B.; Zou, J.; Amal, R. *Adv. Funct. Mater.* **2009**, *19*, 369.

(23) Stosser, R.; Marx, U.; Herrmann, W.; Jabor, J. K.; Bruckner, A. *J. Am. Chem. Soc.* **2010**, *132*, 9873.

(24) Waser, O.; Hess, M.; Guntner, A.; Novak, P.; Pratsinis, S. E. *J. Power Sources* **2013**, *241*, 415.

(25) Büchel, R.; Strobel, R.; Baiker, A.; Pratsinis, S. E. *Top. Catal.* **2009**, *52*, 1709.

(26) Madler, L.; Stark, W. J.; Pratsinis, S. E. *J. Mater. Res.* **2002**, *17*, 1356.

(27) Shahin, A. M.; Grandjean, F.; Long, G. J.; Schuman, T. P. *Chem. Mater.* **2005**, *17*, 315.

(28) Qiu, N.; Zhang, J.; Wu, Z. Y.; Hu, T. D.; Liu, P. *Cryst. Growth Des.* **2012**, *12*, 629.

(29) Reijerse, E.; Lendzian, F.; Isaacson, R.; Lubitz, W. *J. Magn. Reson.* **2012**, *214*, 237.

(30) Cox, N.; Lubitz, W.; Savitsky, A. *Molecular Physics* **2013**, *111*, 2788.

(31) Nalepa, A.; Möbius, K.; Lubitz, W.; Savitsky, A. *J. Magn. Reson.* **2014**, *242*, 203.

(32) Rapatskiy, L.; Cox, N.; Savitsky, A.; Ames, W. M.; Sander, J.; Nowaczyk, M. M.; Rögner, M.; Boussac, A.; Neese, F.; Messinger, J.; Lubitz, W. *J. Am. Chem. Soc.* **2012**, *134*, 16619.

(33) Yen, H.; Seo, Y.; Kaliaguine, S.; Kleitz, F. *Angew. Chem. Int. Ed.* **2012**, *51*, 12032.

(34) Zabilskiy, M.; Djinovic, P.; Tchernychova, E.; Tkachenko, O. P.; Kustov, L. M.; Pintar, A. *ACS Catal.* **2015**, *5*, 5357.

(35) Landi, G.; Barbato, P. S.; Benedetto, A. D.; Lisi, L. *Appl. Catal. B-Environ.* **2016**, *181*, 727.

(36) Harrison, P. G.; Ball, I. K.; Azelee, W.; Daniell, W.; Goldfarb, D. *Chem. Mater.* **2000**, *12*, 3715.

(37) Getz, D.; Silver, B. L. *J. Chem. Phys.* **1974**, *61*, 630.

(38) Park, E. D.; Lee, D.; Lee, H. C. *Catal. Today* **2009**, *139*, 280.

(39) Gu, D.; Jia, C. J.; Bongard, H.; Spliethoff, B.; Weidenthaler, C.; Schmidt, W.; Schuth, F. *Appl. Catal. B-Environ.* **2014**, *152*, 11.

(40) Velez, R. P.; Ellmers, I.; Huang, H. M.; Bentrup, U.; Schunemann, V.; Grunert, W.; Bruckner, A. *J. Catal.* **2014**, *316*, 103.

(41) Moreno-Gonzalez, M.; Hueso, B.; Boronat, M.; Blasco, T.; Corma, A. *J. Phys. Chem. Lett.* **2015**, *6*, 1011.

(42) Bruckner, A. *Chem.-Ing.-Tech.* **2014**, *86*, 1871.

Table of Contents